Check for updates

MnO2 coated multi-layer nanoplatform for enhanced sonodynamic therapy and MR imaging of breast cancer

Yan Xu[1,2], Wanlin Tan[1,2], Mingyu Chen[1,2], Sijie Chen[1,2], Kui Tang[1,2], Haiqin Liao[1,2] and Chengcheng Niu[1,2]*

[1]Department of Ultrasound Diagnosis, The Second Xiangya Hospital, Central South University, Changsha, Hunan, China, [2]Research Center of Ultrasonography, The Second Xiangya Hospital, Central South University, Changsha, Hunan, China

Sonodynamic therapy (SDT) is a promising new anti-tumor therapy that inhibits tumor growth by ultrasound activation of sonosensitizers to produce reactive oxygen species (ROS). However, the problems of hypoxia in the microenvironment within solid tumors and the effectiveness of SDT will decrease due to the little accumulation of sonosensitizers at the tumor site, as well as tumor cell tolerance, have limited the development of SDT. To overcome these problems, a core-shell structured nanoparticle (IR780/PLGA@ MnO2 NPs) loaded with IR780 and manganese dioxide (MnO2) was developed as a nanocarrier to transport the sonosensitizer IR780 and the generated oxygen into the tumor tissue. The MnO2 shell layer of IR780/PLGA@MnO2 NPs can prevent the premature release of IR780 in the blood and also it can react with acidic and high H2O2, the generated oxygen can relieve tumor tissue hypoxia, and the generated Mn can enhance magnetic resonance imaging (MRI) signal intensity by acting as a contrast agent for MRI. More importantly, the released IR780 can produce ROS to kill tumor cells under ultrasound excitation. This PH-responsive and H2O2-triggered SDT based on the IR780/PLGA@MnO2NPs is an effective platform to inhibit tumor growth with negligible systemic toxicity. This work develops a multifunctional therapeutic integrated nanoplatform for breast cancer treatment, which is expected to be used in the clinic.

KEYWORDS

sonodynamic therapy, magnetic resonance imaging, tumor hypoxia, reactive oxygen species, manganese dioxide

Introduction

Advances in cancer diagnosis and therapy have attracted immense attention in achieving accurate treatment to minimize side effects and improving the survival rate of patients. Ultrasound (US), as a mechanical wave, is widely used in clinical US imaging for cancer diagnosis and high-intensity focused US for cancer therapy (Wu et al., 2005; Wells, 2006; Hussain and Nguyen, 2014). Moreover, US could facilitate both the drug release and cellular uptake by inducing reversible cell deformation and membrane

permeabilization (Ahmadi et al., 2020). In recent years, sonodynamic therapy (SDT), based on US, as a non-invasive treatment in promoting malignant tumor deterioration, has led to burgeoning research interest, which has the distinct advantages of deep penetration, low cost and low toxicity (Wood and Sehgal, 2015; Qian et al., 2016; Wan et al., 2016). SDT employs activating sonosensitizers through US and utilizes oxygen molecules of tissues into toxic reactive oxygen species (ROS), which can oxidize crucial biomacromolecules such as proteins, enzymes, DNA of tumor cells, thus inhibiting the tumor growth (Rosenthal et al., 2004; Costley et al., 2015; Zhang et al., 2019; Son et al., 2020; Wang et al., 2020). However, the organic sonosensitizer molecule hinders its further application of SDT due to low bioavailability and biological instability (Son et al., 2020). To overcome these limitations, our previous studies have found that loading the organic sonosensitizer such as IR780 or ICG onto polymeric PLGA could effectively improve the biocompatibility and biological stability (Niu et al., 2017; Wang et al., 2018; Chen et al., 2020; Huang et al., 2020; Pei et al., 2020; Xu et al., 2020).

SDT progress requires enough oxygen molecules in the process of cancer cell destruction, however, the tumor hypoxic microenvironment significantly some inherent resistances to SDT due to the abnormal proliferation of cells, vascular abnormalities, and lymphatic system dysfunction (Hockel and Vaupel, 2001; Dong et al., 2021). Moreover, the high consumption of oxygen in the process of SDT can worsen the hypoxic microenvironment of tumor tissues and conversely influences the therapeutic efficacy of SDT (Wang et al., 2020; Dong et al., 2021). Therefore, how to overcome the limitation of hypoxia in the tumor area on the low ROS-generation efficacy of SDT is a challenging subject. Several strategies have developed to relieve hypoxia, such as using perfluorocarbon to deliver additional oxygen, inhaling supply hyperbaric oxygen, and catalyzing overexpressed hydrogen peroxide (H_2O_2) to O_2 in the tumor tissues (Song et al., 2016a; Song et al., 2016b; Zhu et al., 2018; Huang et al., 2020). Manganese dioxide (MnO_2) and its various nanocomposites, as a catalase-like nanoenzyme to product oxygen by the decomposition of excess H_2O_2 in tumor area is the most effective way to relieve hypoxia, have been attracting increasing attention (Chu et al., 2017; Zhu et al., 2018; Zhang et al., 2020; Zhang and Ji, 2020). Thus, utilizing tumor PH- and H_2O_2- sensitive MnO_2 to relieve hypoxia is promising way, the process of MnO_2 at mild acid and excess H_2O_2 condition can be expressed by the following reactions (Gordijo et al., 2015):

$$MnO_2 + H_2O_2 + 2H^+ \rightarrow Mn^{2+} + H_2O + O_2$$
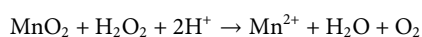
Many studies have already manifested that nanostructured MnO_2 can be act as a catalyst to react with overexpressed H_2O_2 in tumor microenvironment to produce O_2, which could surmount hypoxia in tumor area (Zhu et al., 2018; Yang et al., 2019; Liu et al., 2021). In addition, the process of nanostructured MnO_2

can generate water-soluble Mn^{2+} ions which can be used as an excellent magnetic resonance imaging (MRI) contrast agent for early and accurate diagnosis of cancer (Huang et al., 2017; Liu et al., 2018; Fu et al., 2019; Ding et al., 2020). Furthermore, nanostructured MnO_2 can also assemble anticancer drug molecules and release them when itself degrade in an acidic environment, which could be used as "gatekeeper" carrier for drug delivery (Ma et al., 2017).
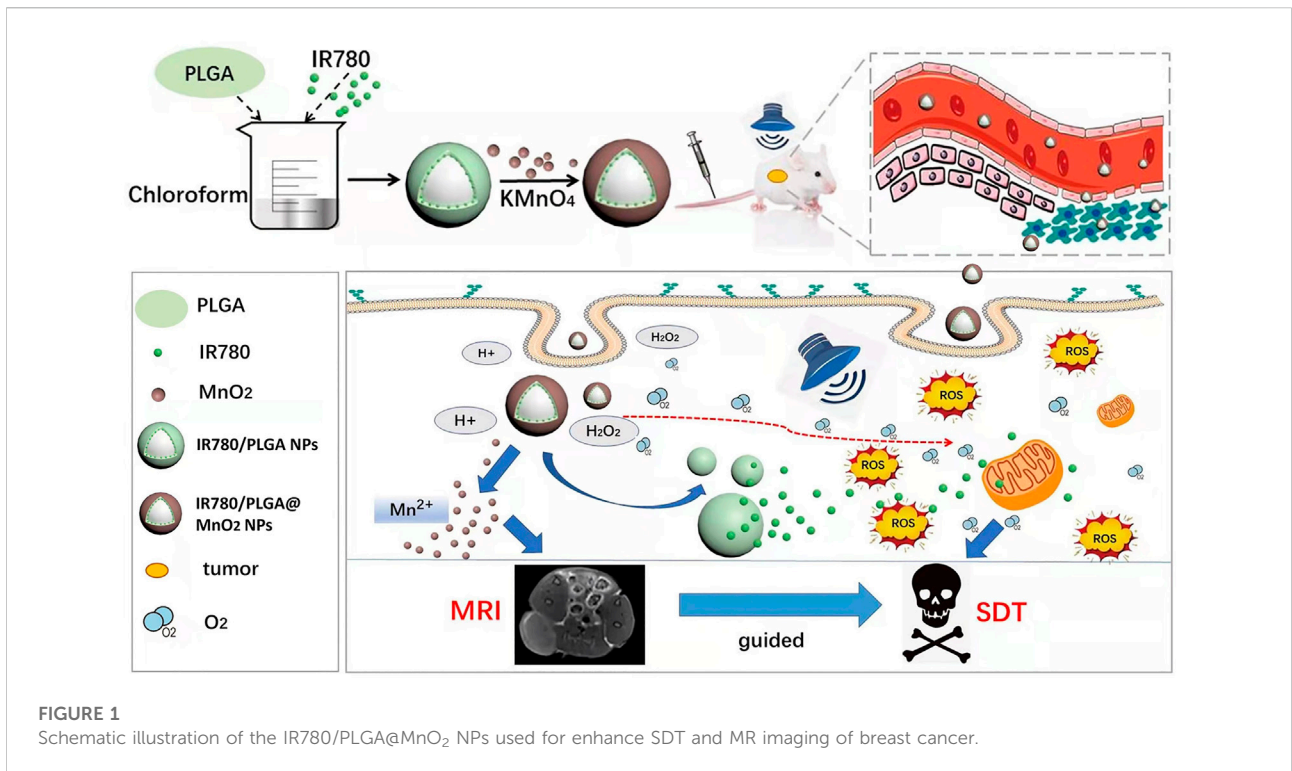
Therefore, we designed a core-shell structure multi-layer nanoparticle (IR780/PLGA@MnO_2 NPs) as sonosensitizer carrier and the oxygen reservoir to enhance the efficacy of SDT and MR imaging (Figure 1). Meanwhile, the MnO_2 shell layer of these IR780/PLGA@MnO_2 NPs could prevent IR780 release in the blood circulation, while react with H^+ and H_2O_2 in the tumor area, then decomposing and releasing the IR780 from IR780/PLGA@MnO_2 NPs. Finally, the generation of oxygen could relieve tumor hypoxia, making the exhibit higher ROS generation efficiency even under hypoxia atmosphere, the generation of Mn^{2+} ions could act as the contrast agents for T1-weighted magnetic resonance imaging (MRI) for the recognition and diagnosis of tumor. Thus, the developed IR780/PLGA@MnO_2 NPs would be a potential nanoplatform for controllable tumor oxygenation and MRI-guided tumor-growth suppression.

Materials and methods

Preparation and characterization of IR780/PLGA@MnO_2 NPs

Firstly, 200 mg PLGA and 6 mg IR780 was fully dissolved in 6 ml chloroform, then the above mixture was put into 30 ml PVA (4%) solution, emulsified for 2 min using an ultrasonic processor (5 s on and 5 s off), 20 ml deionized water was added into the mixture and stirred for 12 h in order to volatilize the chloroform. Then, the resulting IR780/PLGA NPs was washed with deionized water at least 3 times. To form layered manganese oxide, the prepared IR780/PLGA NPs were dispersed in 100 ml deionized water, then 300 mg potassium permanganate was added, the resulting IR780/PLGA @MnO2 NPs was stirred for 6 h in dark place, washed with deionized water at least 3 times, and kept at 4°C in dark place.

The morphology, structure and element mapping of the IR780/PLGA@MnO_2 NPs was detected by Transmission electron microscopy (TEM, Hitachi, Ltd., Japan), the size and zeta potential of the NPs were tested by dynamic light scattering (DLS, ZEN3600, Malvern Instruments, United Kingdom), and the sizes of the NPs in PBS and 10% fetal bovine serum (FBS) were tested for 7 days to study the size stability. The optical properties of various NPs (PLGA NPs, IR780/PLGA NPs, IR780/ PLGA@MnO_2 NPs) were tested by a UV-vis-NIR spectrophotometer (UV-3600, Shimadzu, Japan). The Mn

FIGURE 1
Schematic illustration of the IR780/PLGA@MnO$_2$ NPs used for enhance SDT and MR imaging of breast cancer.

content was calculated by ICP-OES (ICP-OES730, Agilent Co. Ltd., USA). The amount of IR780 encapsulated into the IR780/PLGA@MnO$_2$ NPs were recorded by a UV-vis-NIR spectrophotometer.

Oxygen Storage and IR780 Release from the IR780/PLGA@MnO$_2$ NPs in Response to H$_2$O$_2$

A dissolved oxygen meter (AMT08, United States) was used to measure the O$_2$ concentration of IR780/PLGA@MnO$_2$ NPs in response to H$_2$O$_2$. Ten milliliters of deoxygenated water with H$_2$O$_2$ (25 μM), IR780/PLGA NPs or IR780/PLGA@MnO$_2$ NPs were loaded into a glass bottle. The real-time O$_2$ concentration in the bottle was recorded every 10 s, the IR780 release experiment of the IR780/PLGA@MnO$_2$ NPs was recorded by a UV-vis-NIR spectrophotometer. The IR780/PLGA@MnO$_2$ NPs were loaded into dialysis bags (1 ml) and put into different buffers, including PBS (pH 7.4) and PBS (pH 5.5) with 25 μM H$_2$O$_2$, PBS (pH 5.5) without 25 μM H$_2$O$_2$ to partially mimic the microenvironments of healthy tissue and tumor tissue. At the different time points up to 72 h, IR780 concentration of each time point was recorded according to the standard curve of IR780.

Measurement of ROS generation *in vitro*

SOSG was used as a fluorescent probe to measure the production of ^{1}O$_2$, 1 ml of IR780/PLGA@MnO$_2$ NPs (100 μg/ml) and 1 μL of (SOSG, 5 μM) was irradiated by US transducer at an ultrasonic intensity of 1 W/cm^2 with the duty cycle of 40% in different time (0, 30, 60, 90, 120, 150 or 180 s). The SOSG fluorescence was tested by a fluorescence spectrometer (Tecan, Männedorf, Switzerland) for IR780/PLGA@MnO$_2$ NPs, H$_2$O$_2$ and IR780/PLGA NPs, the relative efficiency of ^{1}O$_2$ production was calculated by F1 (under US irradiation)/F0 (before US irradiation).

Intracellular uptake

4T1 mice breast cancer cells were cultured at 37°C in RPMI-1640 medium containing 10% (v/v) FBS, 1% (v/v) penicillin G and streptomycin, 4T1 cells (1×10^4 cells/well) were seeded on laser confocal petri dish for 24 h. Then, DiI labeled IR780/PLGA@MnO$_2$ NPs (200 μL, 1 mg/ml) were added and co-incubated for 0, 4, 12 and 24 h, washed for 3 times in dark, fixed with 4% paraformaldehyde for 15 min and stained with DAPI for 5 min. Finally, the cells were observed by a laser confocal microscope.

Cellular reactive oxygen species generation

DCFH-DA cellular ROS assay kit was used to detect intracellular ROS production. 4T1 cells (1×10^5 cells/well) were seeded in the 6-well plates and treated with different conditions: (Hussain and Nguyen, 2014) PBS, (Wells, 2006) US, (Wu et al., 2005) IR780/PLGA NPs, (Ahmadi et al., 2020) IR780/PLGA NPs + US, (Qian et al., 2016) IR780/PLGA@MnO$_2$ NPs, (Wood and Sehgal, 2015) IR780/PLGA@MnO$_2$ NPs + US. The intensity of US is 1.0 W/cm^2 and the time is 2 min, the NPs concentration is 1.0 mg/ml and the dosage is 200 μL. After incubation for 24 h, DCFH-DA (10 μM) was added to each well, ROS production was determined by fluorescence microscopy.

Cell viability assay

Mice breast cancer 4T1 cells and human breast cancer MCF-7 cells (5×10^3 cells/well) were seeded in a 96-well plate and cultured overnight under normoxic or hypoxic conditions, respectively. To test the cell viabilities of different IR780/PLGA@MnO$_2$ NPs concentrations, 50 μL of IR780/PLGA@MnO$_2$ NPs with different concentrations (1.65, 3.25, 6.25, 12.5, 25.0, and 50.0 μg/ml) were added into the each well and incubated overnight, respectively, then the cell viability was calculated with a CCK-8 cytotoxicity assay kit. To test the cell viabilities of different treatments under normoxic or hypoxic conditions, cells were randomly divided into six groups: (Hussain and Nguyen, 2014) PBS, (Wells, 2006) US, (Wu et al., 2005) IR780/PLGA NPs, (Ahmadi et al., 2020) IR780/PLGA NPs + US, (Qian et al., 2016) IR780/PLGA@MnO$_2$ NPs, (Wood and Sehgal, 2015) IR780/PLGA@MnO$_2$ NPs + US. The intensity of US is 1.0 W/cm^2, the time is 2 min The NPs concentration is 6.25 μg/ml and the dosage is 50 μL. After 24 h of incubation, the cell viability was determined using a CCK-8 cytotoxicity assay kit.

Apoptosis assay

4T1 cells (1×10^5 cells/well) were seeded in the 6-well plates and cultured for 24 h. The cells were treated with different conditions: (Hussain and Nguyen, 2014) PBS, (Wells, 2006) US, (Wu et al., 2005) IR780/PLGA NPs, (Ahmadi et al., 2020) IR780/PLGA NPs + US, (Qian et al., 2016) IR780/PLGA@MnO$_2$ NPs, (Wood and Sehgal, 2015) IR780/PLGA@MnO$_2$ NPs + US. The intensity of US is 1.0 W/cm^2, the time is 2 min, the NPs concentration is 1.0 mg/ml and the dosage is 200 μL. Then the cells were washed 3 times and stained with PI and DAPI, and observed by fluorescence microscopy.

Animal model

Female BALB/c mice (6 weeks old, 20 g) were obtained from the Hunan Silaike Laboratory Animal Corporation (Changsha, China). 4T1 cells (1×10^6) were injected into the mice by subcutaneous injection to establish a breast tumor model when the tumor volume reached 80 mm^3. All animal experiments were approved by the Ethics Committee of the Second Xiangya Hospital of Central South University and conducted in accordance with the guidelines of the Department of Laboratory Animals of Central South University.

Biodistribution and biosafety

For evaluating the biodistribution of IR780/PLGA@MnO$_2$ NPs, 15 tumor-bearing BALB/c mice ($n = 3$) were injected with 200 μL of IR780/PLGA@MnO$_2$ NPs (1.0 mg/ml) *via* the tail vein (0, 4, 8, 12, 24 h before imaging) for *in vivo* fluorescent imaging (Ex: 745 nm, Em: 840 nm) by a Lumina IVIS Spectrum imaging system (PerkinElmer, United States). Mice of each group were sacrificed after the whole-body imaging, then the major organs and tumor were taken out for *in vitro* imaging and the average fluorescence intensity was further analyzed.

To further assess the biotoxicity of IR780/PLGA@MnO$_2$ NPs *in vivo*, 10 tumor-bearing BALB/c mice ($n = 5$) were randomly divided into 2 groups: (Hussain and Nguyen, 2014) saline and (Wells, 2006) IR780/PLGA@MnO$_2$ NPs. Mice in the two groups were injected with 200 μL of saline or IR780/PLGA@MnO$_2$ NPs (2.0 mg/ml) *via* the tail vein, then the H&E stain of main organs was observed after 14 days injection.

MR imaging *in vitro* and *in vivo*

MR imaging *in vitro* were tested on a clinical by MRI instrument (UR770 3.0T, United imaging Ltd., China) equipped with a small animal coil. Different MnO$_2$ concentrations (Mn concentrations: 0.00, 0.05, 0.10, 0.20, 0.30, and 0.40 mM) of the IR780/PLGA@MnO2 NPs were dispersed in different media: (Hussain and Nguyen, 2014) pH 7.4; (Wells, 2006) pH 5.5, 25 μM H$_2$O$_2$. Then, the different concentrations of IR780/PLGA@MnO$_2$ NPs were added to 2 ml Eppendorf tubes for MR imaging (T1 WI). The T1 relaxation time was measured, and the T1 relaxation coefficient (r1) was calculated.

In the *in vivo* T1-weighted MRI experiments, 200 μL of IR780/PLGA@MnO$_2$ NPs solution (2 mg/ml) was intravenously injected into 4T1 tumor-bearing mice. The T1-weighted MR images of tumor sites were captured before and 24 h after injection of IR780/PLGA@MnO$_2$ NPs. Finally, the SI within the ROI of the MR images were measured.
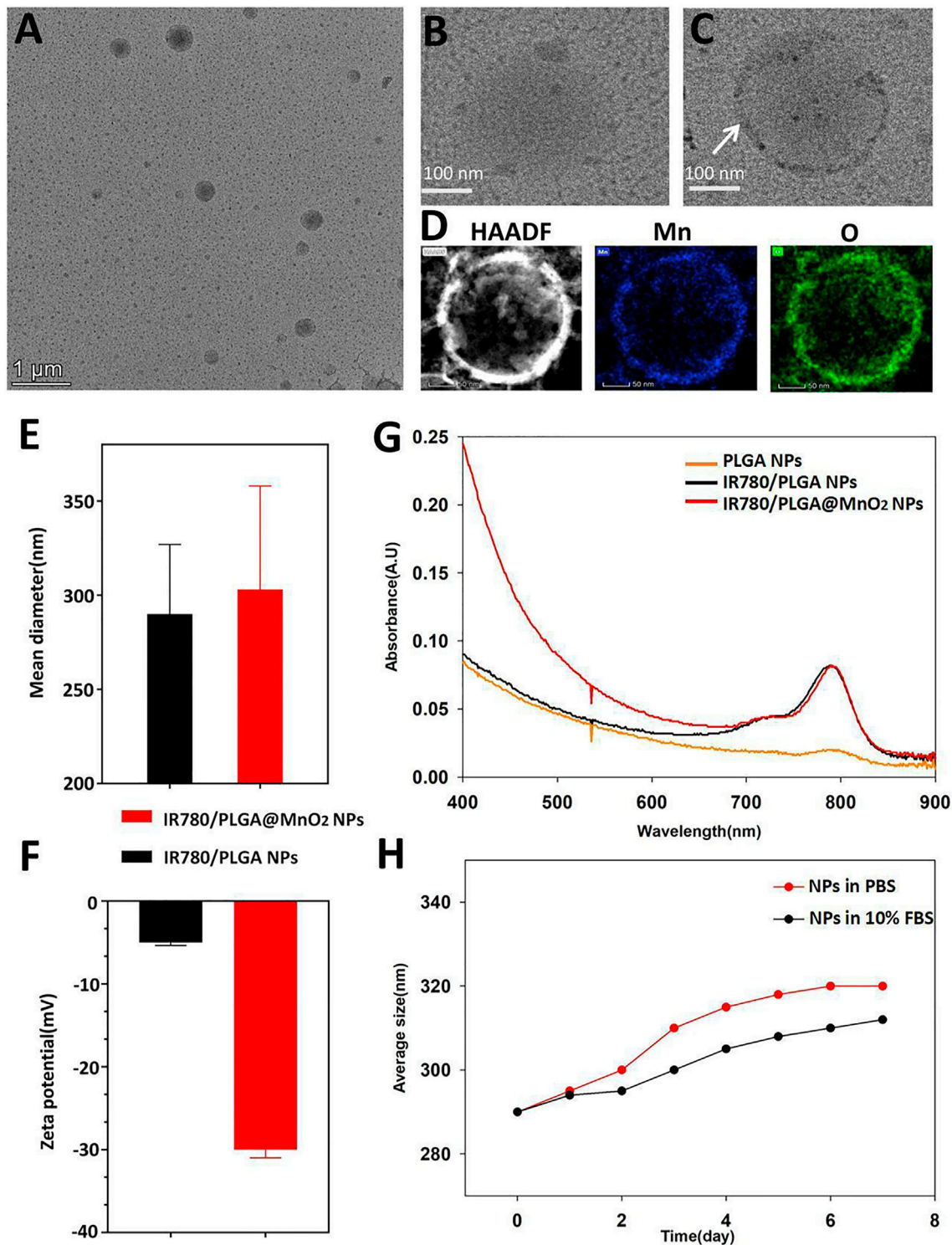
FIGURE 2
Characterization of IR780/PLGA@MnO₂ NPs. **(A–C)** The TEM images of IR780/PLGA@MnO₂ NPs **(A)** and IR780/PLGA NPs **(B)**, the white arrow indicated the MnO₂ on the shell of IR780/PLGA@MnO₂ NPs **(C)**. **(D)** The elemental mapping of Mn and O of IR780/PLGA@MnO**₂.** **(E)** Size and **(F)** zeta potential of IR780/PLGA NPs with and without MnO₂ shell. **(G)** UV–vis–NIR absorption spectra of IR780/PLGA NPs, PLGA NPs, IR780/PLGA@MnO₂ NPs. **(H)** Size distributions of IR780/PLGA@MnO₂ NPs in PBS and 10% FBS for 7 days.

FIGURE 3
(A) The IR780 release from IR780/PLGA@MnO$_2$ NPs at pH 7.4 or 5.5 with or without H$_2$O$_2$. **(B)** Oxygen content of IR780/PLGA MnO$_2$ NPs with H$_2$O$_2$. **(C)** Time-dependent ^{1}O$_2$ generation of IR780/PLGA MnO$_2$ NPs irradiated by US (1 MHz, 1.0 W/cm^2). **(D)** Time-dependent fluorescence increasement of SOSG with different treatments under ultrasound irradiation.
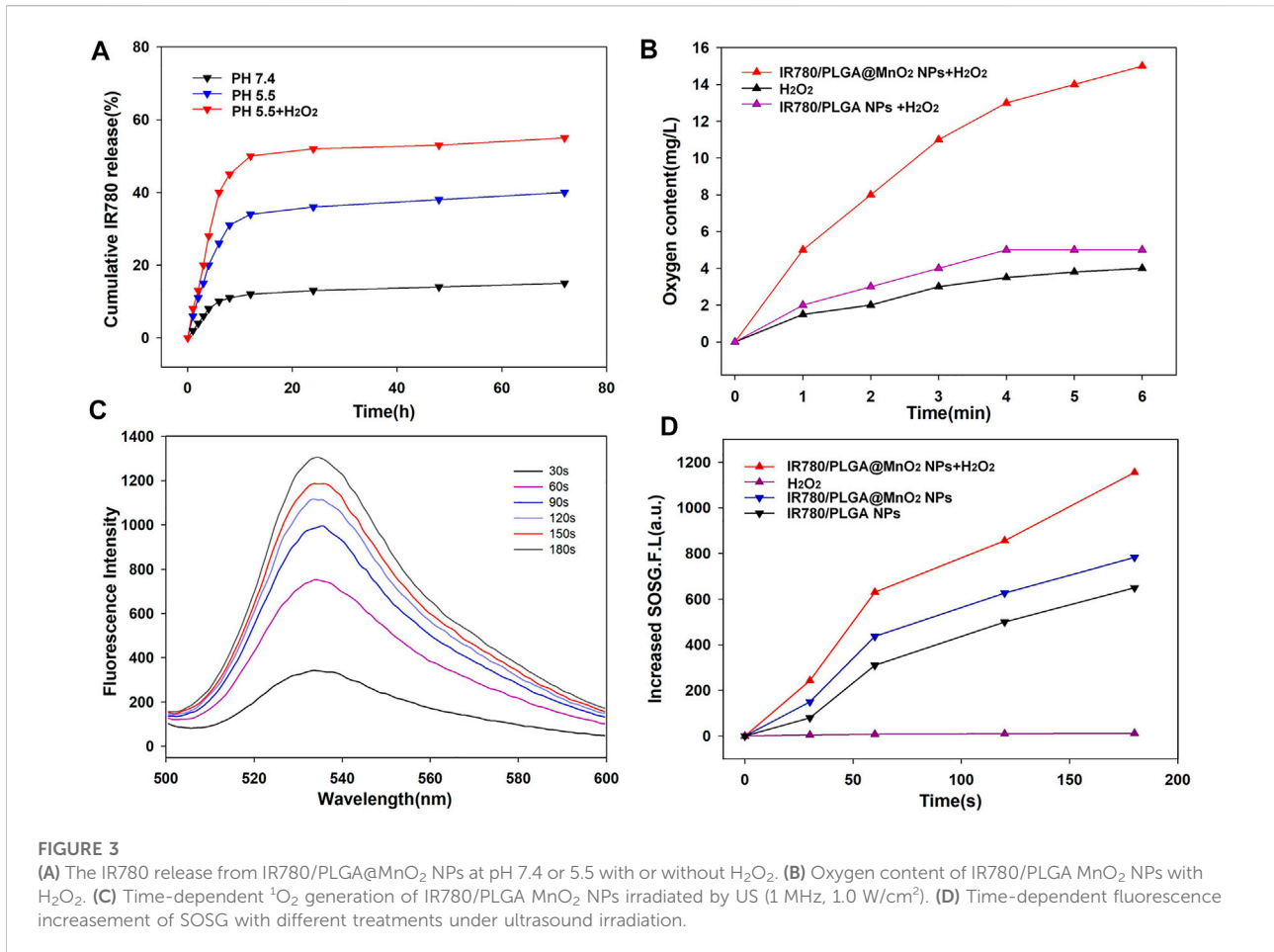
In vivo antitumor effect

To investigate hypoxia environment *in vivo*, the 4T1 tumor-bearing mice (*n* = 5) were randomly divided with different treatments: (Hussain and Nguyen, 2014) saline, (Wells, 2006) IR780/PLGA NPs, (Wu et al., 2005) IR780/PLGA@MnO$_2$ NPs. After 24 h of injection, immunofluorescence of an antibody against hypoxia-inducible factor-1α (HIF-1α) in the tumor was observed.

To investigate the antitumor effect *in vivo*, the 4T1 tumor-bearing mice (*n* = 5) were randomly divided with different treatments: (Hussain and Nguyen, 2014) saline, (Wells, 2006) US, (Wu et al., 2005) IR780/PLGA NPs, (Ahmadi et al., 2020) IR780/PLGA@MnO$_2$ NPs, (Qian et al., 2016) IR780/PLGA NPs + US, (Wood and Sehgal, 2015) IR780/PLGA@MnO$_2$ NPs + US, 200 μL of different NP solutions (2 mg/ml) was intravenously injected into the mice every 2 days. After injection for 8 h, the tumors of the mice in groups (Wells, 2006), (Qian et al., 2016), and (Wood and Sehgal, 2015) were irradiated with US (the ultrasonic intensity is 2 W/cm^2 and duration is 10 min). Body weight and tumor volume were recorded every other day for 14 days. On day 15, the tumors of the mice were obtained. In addition, TUNEL and PCNA immunohistochemical staining were performed on the tumor tissues to observe tumor cell apoptosis and proliferation, respectively.

Statistical analysis

The experimental data were presented as the mean ± SD. Comparisons of two groups were analyzed by Student's t-test and multiple groups were analyzed by two-way analysis using GraphPad Prism 8 software. $p < 0.05$ was considered significant.

Results and discussion

Characterization of IR780/PLGA@ MnO$_2$ NPs

As shown in Figure 2B of the TEM image, spherical IR780/PLGA NPs nanoparticles were successfully constructed. The
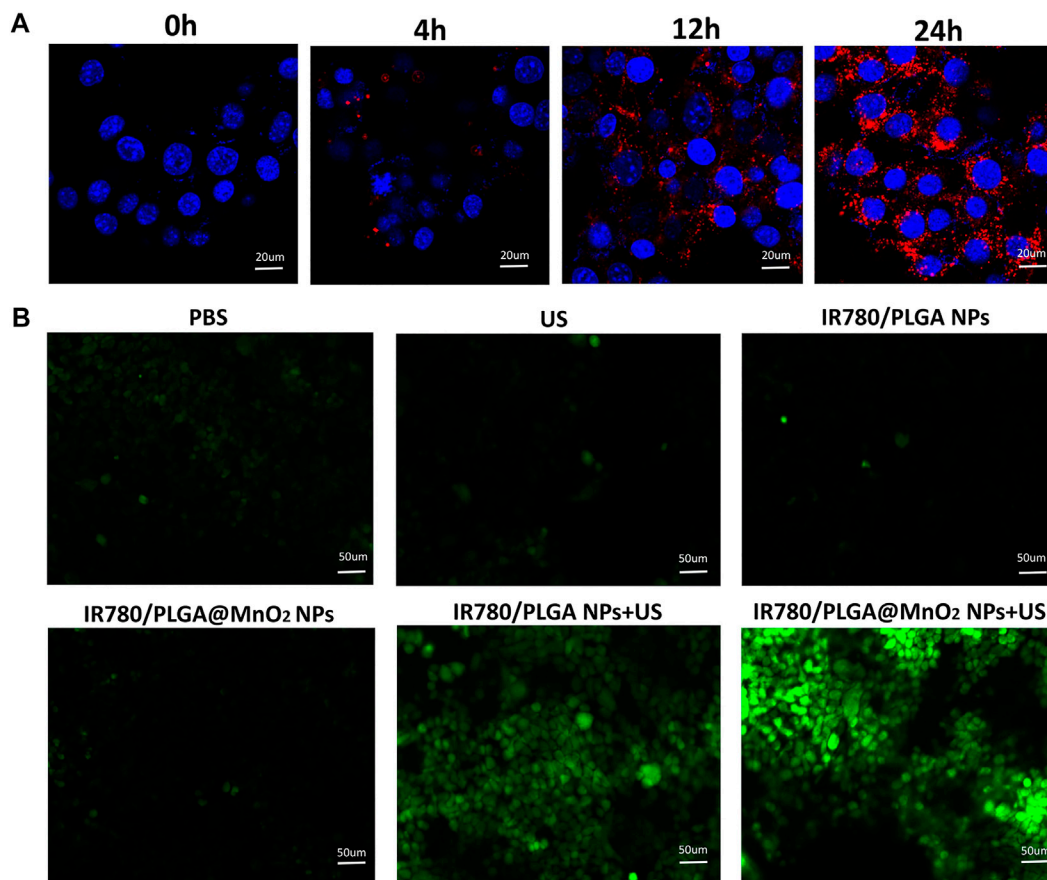
FIGURE 4
(A) Fluorescence images of 4T1 cells incubated with IR780/PLGA@MnO$_2$ NPs for 0, 4, 12 and 24 h (scale bar: 20 μm). **(B)** Fluorescence microscope images of DCFH-DA stained 4T1 cells subjected to different treatments: (Hussain and Nguyen, 2014) PBS, (Wells, 2006) US, (Wu et al., 2005) IR780/PLGA NPs, (Ahmadi et al., 2020) IR780/PLGA@MnO$_2$ NPs, (Qian et al., 2016) IR780/PLGA NPs + US, (Wood and Sehgal, 2015) IR780/PLGA@MnO$_2$ + US (scale bar, 50 μm).

shell of IR780/PLGA@MnO$_2$ NPs coating of MnO$_2$ was proved by TEM images (Figures 2A,C). The elemental mapping of Mn and O of IR780/PLGA@MnO$_2$ (Figure 2D). The size of the IR780/PLGA NPs was approximately 293.05 ± 5.43 nm and increased to 300.34 ± 4.56 nm after MnO$_2$ coating (Figure 2E). The zeta potential decreased from −5.3269 mV to −30.563 mV after MnO$_2$ coating, indicating that the IR780/PLGA@MnO$_2$ NPs is more stable in the blood than the IR780/PLGA NPs (Figure 2F). The UV absorption spectra are shown in Figure 2G, there was an absorption peak at 780–790 nm of the IR780/PLGA@MnO$_2$ NPs, which indicated that the PLGA/IR780@MnO$_2$ NPs was successfully loaded the IR780. The stability of the IR780/PLGA@MnO$_2$ NPs in PBS and 10% FBS solution were shown in Figure 2H. The entrapment efficiency of IR780 in the IR780/PLGA@MnO$_2$ NPs was calculated to be 58.47% ± 1.48%. The Mn content in the IR780/PLGA@MnO$_2$ NPs was approximately 0.2761 mg/ml.

PH and H$_2$O$_2$ responsive IR780 release and responsive oxygen generation

It is known that tumor microenvironment is featured with regional hypoxia, low PH and increasing H$_2$O$_2$ level due to insufficient blood supplement. The MnO$_2$ can react with the increasing H$^+$ and H$_2$O$_2$ in the solid tumor to produce O$_2$ and Mn^{2+} (Sun et al., 2021). When the IR780/PLGA@MnO$_2$ NPs entered the tumor tissue, MnO$_2$ shell gradually dissolved, the IR780/PLGA NPs core exposed, and IR780 release from the IR780/PLGA@MnO$_2$ NPs in the tumor (Figure 3A). Compared with the IR780/PLGA@MnO$_2$ NPs in PBS (pH 7.4), the IR780/PLGA@MnO$_2$ NPs in PBS (pH 5.5) with 25 μM H$_2$O$_2$ exhibited considerably higher IR780 release, and the release rate of IR780 approached 32% within 72 h. For the IR780/PLGA@MnO$_2$ NPs in PBS (pH 5.5) without 25 μM H$_2$O$_2$, the drug release rate was only 20%, revealing that the IR780 release rate was in H$_2$O$_2$ and PH-responsive way.
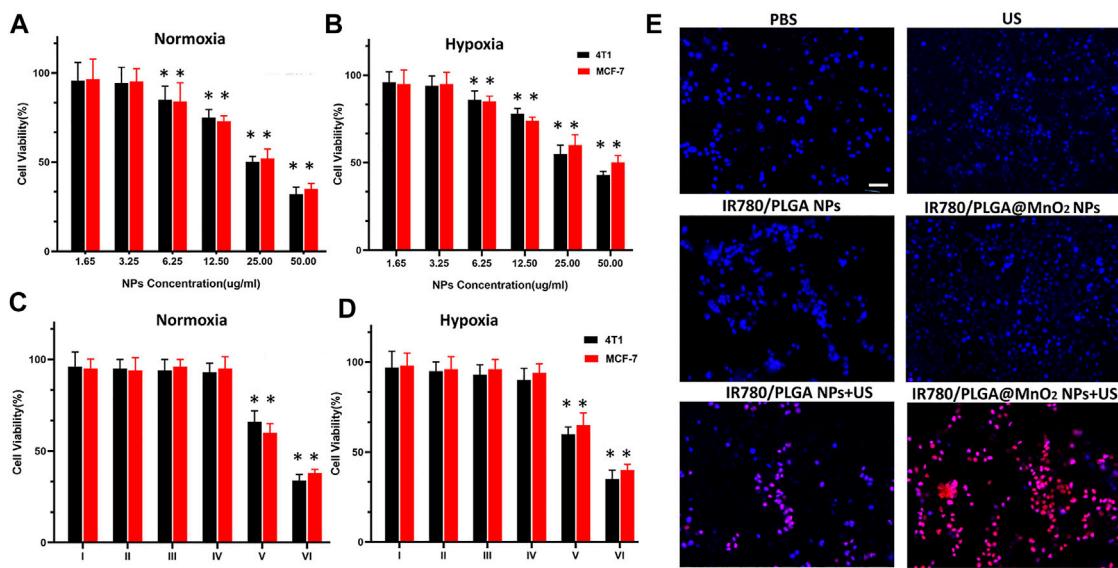
FIGURE 5
(A,B) Cell viability of 4T1 and MCF-7 cells incubated with different concentrations of IR780/PLGA@MnO2 NPs under normoxia environment **(A)** and hypoxia environment **(B)**. **(C,D)** Cell viability of 4T1 and MCF-7 cells under different treatments: (I) PBS, (II) US, (III) IR780/PLGA NPs, (IV) IR780/PLGA@MnO$_2$, (V) IR780/PLGA NPs + US, (VI) IR780/PLGA@MnO$_2$ + US) in normoxia environment **(C)** and hypoxia environment **(D)**. **(E)** Fluorescence microscope images of DAPI and PI co-stained 4T1 cells after various treatments: (Hussain and Nguyen, 2014) PBS, (Wells, 2006) US only, (Wu et al., 2005) IR780/PLGA NPs, (Ahmadi et al., 2020) IR780/PLGA@MnO$_2$ NPs, (Qian et al., 2016) IR780/PLGA NPs + US, (Wood and Sehgal, 2015) IR780/PLGA@MnO$_2$ + US (scale bar, 100 μm). (*p < 0.05, compared with the control group).

The oxygen release profiles of IR780/PLGA@MnO$_2$ NPs were analyzed under hypoxic conditions (Figure 3B). While the IR780/PLGA@MnO$_2$ NPs was dispersed in the deoxygenated medium containing H$_2$O$_2$, the oxygen concentration in water increased from 4 to 13 mg/L water in the first 1 min. Few O$_2$ generation was observed while the IR780/PLGA@MnO$_2$ NPs was dispersed in the deoxygenated medium without H$_2$O$_2$. The oxygen concentration of the IR780/PLGA@MnO$_2$ NPs with H$_2$O$_2$ group was obviously higher than that in the IR780/PLGA@MnO$_2$ NPs without H$_2$O$_2$ group all the time. It means that the oxygen generation the IR780/PLGA@MnO$_2$ NPs with H$_2$O$_2$ was fast and continuous.

Singlet oxygen generation capacity

Based on the efficient oxygen generation of MnO$_2$, SOSG was used as a probe to measure the ^{1}O$_2$ production to assess the SDT effect of the IR780/PLGA@MnO$_2$ NPs with US irradiation. As shown in Figure 3C, at a final IR780/PLGA@MnO$_2$ NPs concentration of 100 μg/ml, the fluorescence intensity of SOSG increased along with the time of US irradiation (0, 60, 120, and 180 s), indicating that the ^{1}O$_2$ production capacity of the IR780/PLGA@MnO$_2$ NPs is outstanding and have the potential against cancer through SDT. As shown in Figure 3D, the fluorescence intensity of SOSG was 819 at 180 s in the IR780/PLGA@MnO$_2$ NPs without H$_2$O$_2$ group. Surprisingly, for the

IR780/PLGA@MnO$_2$ NPs with H$_2$O$_2$, the fluorescence intensity of SOSG was increased as high as 1150. Therefore, more ^{1}O$_2$ generation can be attributed to the increased oxygen concentration from MnO$_2$ which react with H$_2$O$_2$ in the SDT process. These results demonstrated that the IR780/PLGA@MnO$_2$ NPs can effectively generate ^{1}O$_2$ under US irradiation and can be used for sonodynamic treatment of cancer.

Cell uptake and reactive oxygen species determination

To understand the cell uptake of the IR780/PLGA@MnO$_2$ NPs by 4T1 cells, DiI-labeled NPs was used to co-incubation with 4T1 cells for 0, 4, 12, and 24 h. As shown in Figure 4A, an obvious red fluorescence of the IR780/PLGA@MnO$_2$ NPs was observed in 4 h and increased over time, which demonstrated that the longer co-incubation time between the IR780/PLGA@MnO$_2$ NPs and cells, the more nanoparticles phagocytized by 4T1 cells.

To understand intracellular oxidative stress of the IR780/PLGA@MnO$_2$ NPs to examine the sonodynamic activity, DCFH-DA was used as a probe. As shown in Figure 4B, barely green fluorescence was observed in (Hussain and Nguyen, 2014) PBS, (Wells, 2006) US, (Wu et al., 2005) IR780/PLGA NPs and (Ahmadi et al., 2020) IR780/PLGA@MnO$_2$ groups, which suggested that only US irradiation or only NPs cannot produce ^{1}O$_2$. Obvious green
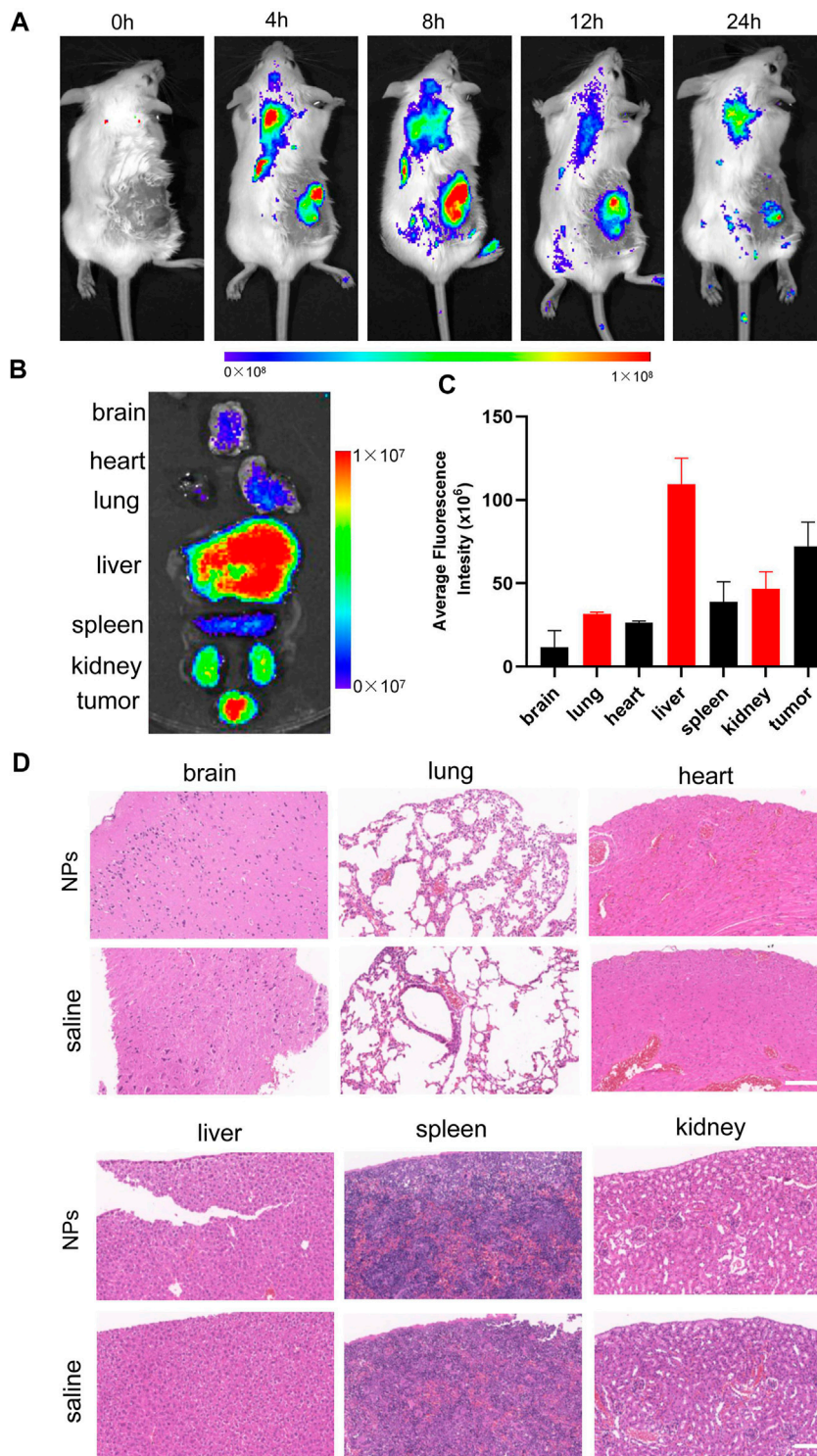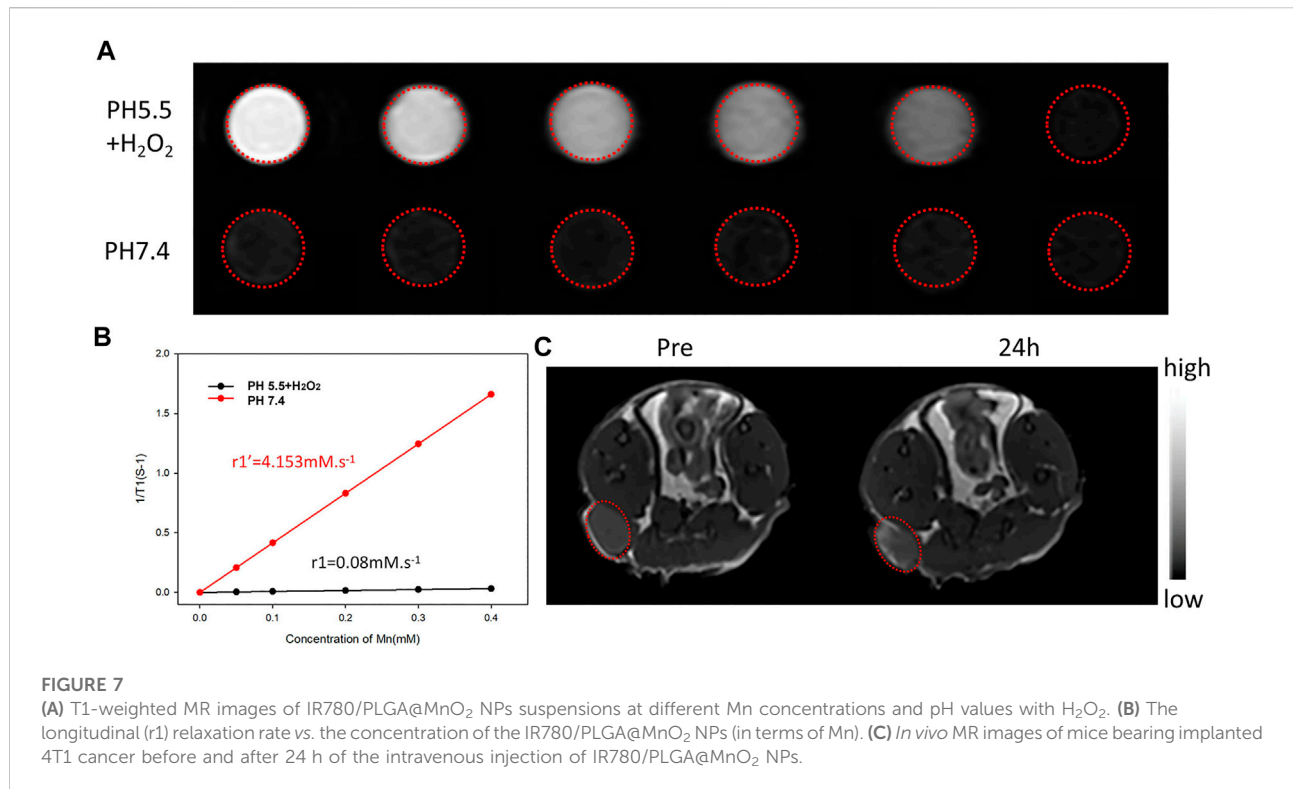
FIGURE 6
(A) Biodistribution of IR780/PLGA@MnO$_2$ NPs in tumor-bearing mice at different time points by *in vivo* fluorescent imaging. **(B,C)** Fluorescence imaging of major organs and tumor at 8 h after injection of the IR780/PLGA@MnO$_2$ NPs. **(D)** H&E-staining images of major organs collected from the IR780/PLGA@MnO$_2$ NPs and saline groups.

FIGURE 7
(A) T1-weighted MR images of IR780/PLGA@MnO$_2$ NPs suspensions at different Mn concentrations and pH values with H$_2$O$_2$. **(B)** The longitudinal (r1) relaxation rate *vs.* the concentration of the IR780/PLGA@MnO$_2$ NPs (in terms of Mn). **(C)** *In vivo* MR images of mice bearing implanted 4T1 cancer before and after 24 h of the intravenous injection of IR780/PLGA@MnO$_2$ NPs.
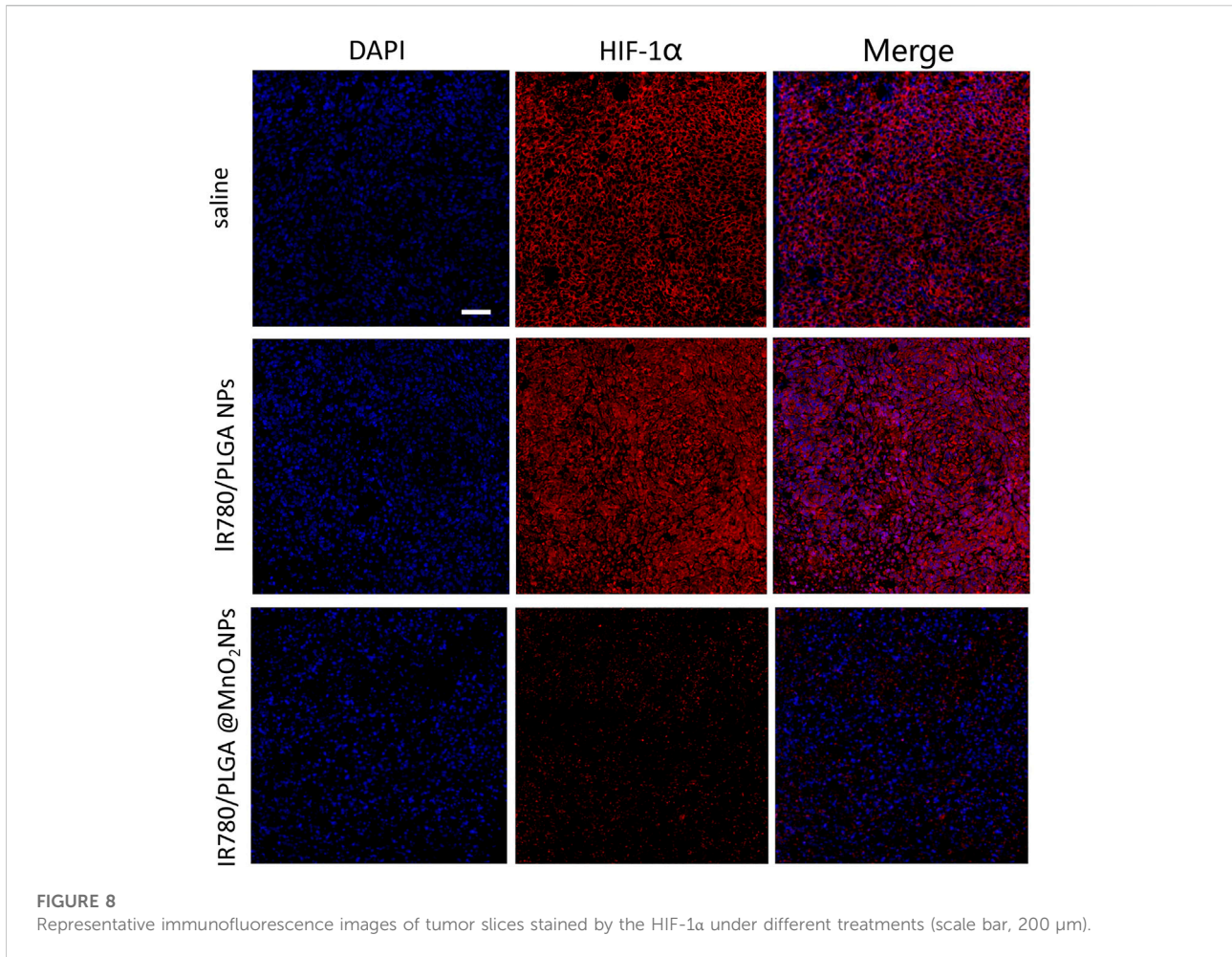
fluorescence was observed in (Qian et al., 2016) IR780/PLGA NPs + US and (Wood and Sehgal, 2015) IR780/PLGA@MnO$_2$ + US groups, which suggested both the NPs and US irradiation were necessary for generation of ^{1}O$_2$. Comparing between groups (Qian et al., 2016) and (Wood and Sehgal, 2015), the group of IR780/PLGA@MnO$_2$ + US irradiation has stronger green fluorescence intensity than the group of IR780/PLGA NPs + US irradiation, which suggested that with the help of MnO$_2$ shell reacting with H$_2$O$_2$, the IR780/PLGA@MnO$_2$ NPs could generate more O$_2$ and then product more ^{1}O$_2$. Therefore, with loading of the shell of MnO$_2$ to provide O$_2$, the IR780/PLGA@MnO$_2$ NPs have excellent properties of SDT against cancer.

In vitro biocompatibility and antitumor activity

Cytotoxicity and antitumor activity of IR780/PLGA@MnO$_2$ NPs under normoxic and hypoxic environments were measured in 4T1 cells and MCF-7 cells. According to CCK8 assay (Figures 5A,B), when the concentration of IR780/PLGA@MnO$_2$ was 0–6.25 μg/ml, the cell survival rate of CCK8 was more than 95% under normoxic and hypoxic conditions, which suggested low toxicity of IR780/PLGA@MnO$_2$ NPs, and 6.25 μg/ml is the appropriate concentration for further biological experiment. When the concentration increased, the cell survival rate of

4T1 cell and MCF-7 cells obviously decreased. To evaluate the antitumor activity of IR780/PLGA@MnO$_2$ NPs through SDT, the 4T1 and MCF-7 viabilities in normoxic and hypoxic environments treated with different conditions was measured (Figures 5C,D). In the normoxic and hypoxic environments, both the 4T1 and MCF-7 cell viabilities of US group were up to 90%, indicating that US exposure (1W/cm^2) is safe to cells. When the IR780/PLGA NPs and IR780/PLGA@MnO$_2$ NPs combined with US exposure, the 4T1 cell viabilities further decreased. Treatment of IR780/PLGA@MnO$_2$ NPs combined with US exposure results in 75% cell death, which was higher than that of IR780/PLGA NPs results in 45% cell death, suggesting that the MnO$_2$ shell coated in IR780/PLGA@MnO$_2$ NPs enhances more cell apoptosis through the SDT effects due to more O$_2$ production.

A live/dead staining assay was used to evaluate the therapeutic efficiency of IR780/PLGA@MnO$_2$ NPs under US irradiation. Blue fluorescence of DAPI stained with all cells and red fluorescence of PI stained with dead cells. As shown in Figure 5E, there is bare red fluorescence in the (Hussain and Nguyen, 2014) PBS, (Wells, 2006) US, (Wu et al., 2005) IR780/PLGA NPs and (Ahmadi et al., 2020) IR780/PLGA@MnO$_2$ NPs groups. Red fluorescence was observed when the cells treated with IR780/PLGA NPs under US irradiation. Furthermore, more red fluorescence was observed in the IR780/PLGA@MnO$_2$ NPs under US irradiation group, which further confirmed that with the help of MnO$_2$ shell respective to

FIGURE 8
Representative immunofluorescence images of tumor slices stained by the HIF-1α under different treatments (scale bar, 200 μm).

H_2O_2 to produce O_2, the SDT efficacy of IR780 is enhanced and suggested that IR780/PLGA@MnO$_2$ NPs is an efficient sonodynamic agent for hypoxic cancer cells under US irradiation.

Biodistribution and biosafety

To evaluate the biodistribution of IR780/PLGA@MnO$_2$ NPs, the *in vivo* fluorescent imaging at different time points were carried out. As shown in Figure 6A, before injection of the IR780/PLGA@MnO$_2$ NPs, there were no red fluorescent signals in the tumor region of tumor bearing mice. Obvious fluorescence was observed at the tumor site after injection 4 h, arrived to the peak intensity at 8 h and maintained until 24 h. The fluorescence of the major organs and tumor after injection 8 h was shown in Figures 6B,C, the IR780/PLGA@MnO$_2$ NPs was mainly accumulated in the tumors and the reticuloendothelial system (such as liver), which was consistent with the previous studies (Chen et al., 2020).

To further assess the biotoxicity of IR780/PLGA@MnO$_2$ NPs *in vivo*, the H&E stain of main organs was observed after 14 days injection. As shown in Figure 6D, there was no apparent changes in pathological damage and inflammation lesion in the major organs (brain, heart, liver, spleen, lung, and kidney) with injection of IR780/PLGA@MnO$_2$ NPs, which proved that IR780/PLGA@MnO$_2$ NPs have low potential toxicity and was biosafe *in vivo* for further tumor SDT.

MR imaging in vitro and in vivo

As we known, because of high spatial resolution and deep tissue penetration, MRI is widely used as an imaging modality in clinical diagnosis. Several manganese dioxide related contrast agents that respond to tumor microenvironment, such as low-pH and excess-H_2O_2, have been reported for enhancement MR imaging. The relaxation properties of IR780/PLGA@MnO$_2$ NPs under different buffer *in vitro* were verified to investigate the MR imaging performance using a 3.0 T clinical MRI scanner. As shown in
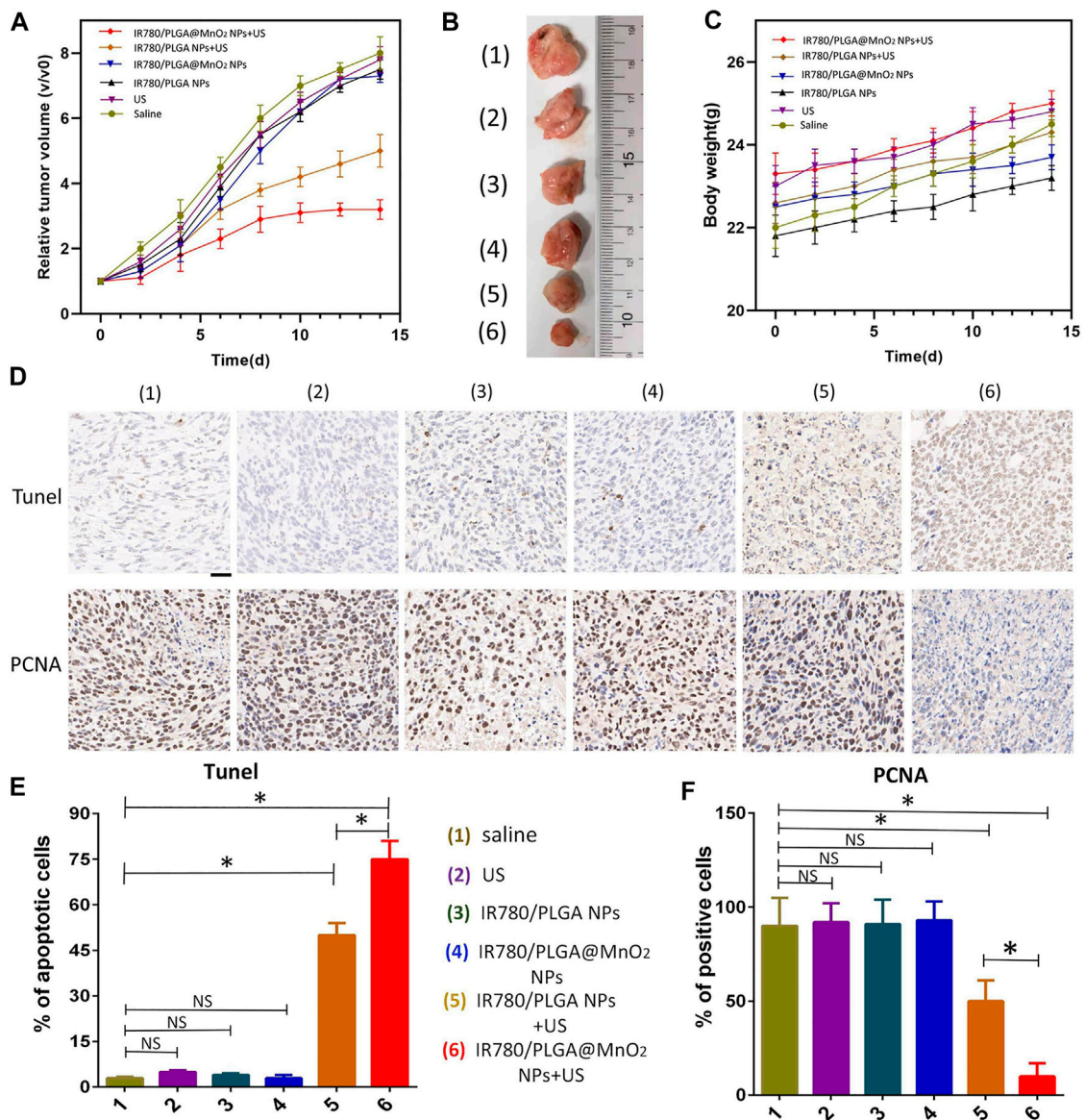
FIGURE 9
(A) The relative tumor growth curves and **(B)** photographs of tumors during the various treatments after 14 days. **(C)** The weight growth curves of different groups of mice after various treatments. **(D)** Microscopy images of TUNEL and PCNA assays of stained tumor tissues at different treatments: (Hussain and Nguyen, 2014) Saline, (Wells, 2006) US, (Wu et al., 2005) IR780/PLGA NPs, (Ahmadi et al., 2020) IR780/PLGA@MnO₂NPs, (Qian et al., 2016) IR780/PLGA NPs + US, (Wood and Sehgal, 2015) IR780/PLGA@MnO₂ NPs + US (scale bar, 200 μm). **(E)** The relative quantification of TUNEL and **(F)** PCNA after different treatments. (*$p < 0.05$).

Figure 7A, in the presence of acid (pH 5.5) and H_2O_2, IR780/PLGA@MnO₂ NPs shows that the brightness of the T1 weighted MR images increased rapidly with the increasing MnO₂ concentration. As the MnO₂ concentration increased, the T1 weighted MR images showed brighter. However, in the presence of the physiological environment pH 7.4, the change of the brightness was small and the increase of the T1 weighted MR images was relatively weaker. Moreover, as shown in Figure 7B, the

T1 relaxation coefficient (r1) is also increased from 0.08×10^{-3} m/s (pH 7.4) to 4.1×10^{-3} m/s (pH 5.0 and H_2O_2), which demonstrated that IR780/PLGA@MnO₂ NPs can be used as tumor microenvironment stimulate-responsive T1 MRI contrast agents.

Then the T1-weighted MRI of the tumor before and after 24 h injection of IR780/PLGA@MnO₂ NPs *in vivo* was investigated. As shown in Figure 7C, compared with before injection, the tumor area turned bright after injection of IR780/PLGA@MnO₂ NPs and the

signal intensity (SI) in the tumor area obviously increased at 24 h after injection, which indicated that IR780/PLGA@MnO$_2$ NPs can accumulate at the tumor site and have the capability of tumor microenvironment -activated MR imaging.

In vivo tumor hypoxia environment after different treatments

Tumor hypoxia plays an important role in SDT resistance, angiogenesis and invasiveness of tumor, the hypoxic tumor microenvironment highly express hypoxia-inducible factors (HIFs). In this study, the capability of O$_2$ production *via* IR780/PLGA@MnO$_2$ NPs to relieve tumor hypoxia *in vitro* were confirmed. Then, *in vivo*, a HIF-1α probe was used to verify the tumor hypoxia with different treatments by immunofluorescence assay. As shown in Figure 8, there was strong red fluorescence in the saline and IR780/PLGA NPs groups, which suggested obvious hypoxia tumor conditions. Comparatively, the red fluorescence of the group treated with IR780/PLGA@MnO$_2$ NPs was much weaker, which demonstrated that tumor hypoxia was relieved by IR780/PLGA@MnO$_2$ NPs due to O$_2$ production by MnO$_2$.

Antitumor efficacy *in vivo*

The effectiveness of SDT therapy of the IR780/PLGA@MnO$_2$ NPs *in vivo* were investigated. There were 6 groups with different treatments: (Hussain and Nguyen, 2014) saline, (Wells, 2006) US irradiation, (Wu et al., 2005) IR780/PLGA NPs, (Ahmadi et al., 2020) IR780/PLGA@MnO$_2$ NPs, (Qian et al., 2016) IR780/PLGA NPs + US, (Wood and Sehgal, 2015) IR780/PLGA@MnO$_2$ NPs + US. As shown in Figure 9A, after 14 days of treatments, the tumor volumes increased rapidly in the saline, US irradiation, IR780/PLGA@MnO$_2$ NPs groups with 6-, 6.5-, 7-fold increase of the average tumor volumes, respectively. The tumor volume increased 5.5-fold in the group of IR780/PLGA NPs and US irradiation. However, the growth of tumors is slowly increased in the group of IR780/PLGA@MnO$_2$ NPs and US irradiation. Figure 9B showed photographs of tumors during the various treatments after 14 days, indicating that the IR780/PLGA@MnO$_2$ NPs combined with US irradiation could inhibit tumor growth through SDT and that the effectiveness against tumor of IR780/PLGA NPs coated with MnO$_2$ was better than the IR780/PLGA NPs without MnO$_2$. As shown in Figure 9C, there was bare weight loss of the mice in the 6 groups, which implied the good biosafety of PLGA/IR780@MnO$_2$ NPs and US. The therapeutic efficacy of SDT was further evaluated by the TUNEL and PCNA assays of the tumor tissues. As shown in Figures 9D,E, compared with the groups of (Hussain and Nguyen, 2014) saline, (Wells, 2006) US irradiation, (Wu et al., 2005) IR780/PLGA NPs and (Ahmadi et al., 2020) IR780/PLGA@MnO$_2$ NPs, the proliferative cells with brown nuclear staining of the TUNEL assay of the (Qian et al., 2016) IR780/PLGA NPs + US group was higher, but they were lower than that in

the (Wood and Sehgal, 2015) IR780/PLGA@MnO$_2$ NPs + US group. Opposite to the TUNEL expression pattern, the proliferative cells with brown nuclear staining of PCNA expression were the lowest in the (Wood and Sehgal, 2015) IR780/PLGA@MnO$_2$ NPs + US group (Figures 9D,F). These results indicated that the PH-responsive and H$_2$O$_2$-triggered SDT based on the IR780/PLGA@MnO$_2$NPs is an effective platform to inhibit tumor growth with negligible systemic toxicity.

Conclusion

In summary, we successfully developed a multi-layer core-shell nanostructure of IR780/PLGA@MnO$_2$ NPs with a high IR780-loading and low-leaking, which enhanced the SDT effect of 4T1 tumor bearing mice by deep penetration, H$_2$O$_2$-sensitive oxygen supply, under the guidance of MRI imaging. Introduction of the MnO$_2$ shell can be react with overexpressed acidic H$_2$O$_2$ of tumor site to product Mn^{2+} for MRI and generate O$_2$ for the improvement of hypoxia for enhanced SDT. We believe that our design of the IR780/PLGA@MnO$_2$ NPs as a tumor microenvironment-sensitive nanoplatform provides a promising strategy for cancer diagnosis and SDT treatment, which could be further applied for cancer theranostics.

Data availability statement

The original contributions presented in the study are included in the article/supplementary material, further inquiries can be directed to the corresponding author.

Ethics statement

The animal study was reviewed and approved by the Ethics Committee of Second Xiangya Hospital, Central South University, China.

Author contributions

Conceptualization, CN and YX; methodology and investigation, YX, WT, MC, SC, KT, and HL; writing-original draft, YX; writing-review and editing, CN; supervision, CN; funding acquisition, YX and CN. All authors read and approved the final manuscript.

Funding

Conflict of interest

The authors declare that the research was conducted in the absence of any commercial or financial relationships that could be construed as a potential conflict of interest.

Publisher's note

All claims expressed in this article are solely those of the authors and do not necessarily represent those of their affiliated organizations, or those of the publisher, the editors and the reviewers. Any product that may be evaluated in this article, or claim that may be made by its manufacturer, is not guaranteed or endorsed by the publisher.

References

Ahmadi, A., Hosseini-Nami, S., Abed, Z., Beik, J., Aranda-Lara, L., Samadian, H., et al. (2020). Recent advances in ultrasound-triggered drug delivery through lipid-based nanomaterials. *Drug Discov. Today* 25 (12), 2182–2200. doi:10.1016/j.drudis.2020.09.026

Chen, S., Huang, B., Pei, W., Wang, L., Xu, Y., and Niu, C. (2020). Mitochondria-targeting oxygen-sufficient perfluorocarbon nanoparticles for imaging-guided tumor phototherapy. *Int. J. Nanomedicine* 15, 8641–8658. doi:10.2147/IJN.S281649

Chu, C., Lin, H., Liu, H., Wang, X., Wang, J., Zhang, P., et al. (2017). Tumor microenvironment-triggered supramolecular system as an *in situ* nanotheranostic generator for cancer phototherapy. *Adv. Mat.* 29 (23), 1605928. doi:10.1002/adma.201605928

Costley, D., Mc Ewan, C., Fowley, C., McHale, A. P., Atchison, J., Nomikou, N., et al. (2015). Treating cancer with sonodynamic therapy: A review. *Int. J. Hyperth.* 31 (2), 107–117. doi:10.3109/02656736.2014.992484

Ding, B., Zheng, P., Ma, P., and Lin, J. (2020). Manganese oxide nanomaterials: Synthesis, properties, and theranostic applications. *Adv. Mat.* 32 (10), e1905823. doi:10.1002/adma.201905823

Dong, C., Hu, H., Sun, L., and Chen, Y. (2021). Inorganic chemoreactive nanosonosensitzers with unique physiochemical properties and structural features for versatile sonodynamic nanotherapies. *Biomed. Mat.* 16 (3), 032006. doi:10.1088/1748-605X/abef58

Fu, C., Duan, X., Cao, M., Jiang, S., Ban, X., Guo, N., et al. (2019). Targeted magnetic resonance imaging and modulation of hypoxia with multifunctional hyaluronic acid-MnO2 nanoparticles in glioma. *Adv. Healthc. Mat.* 8 (10), e1900047. doi:10.1002/adhm.201900047

Gordijo, C. R., Abbasi, A. Z., Amini, M. A., Lip, H. Y., Maeda, A., Cai, P., et al. (2015). Design of hybrid MnO2-polymer-lipid nanoparticles with tunable oxygen generation rates and tumor accumulation for cancer treatment. *Adv. Funct. Mat.* 25 (12), 1858–1872. doi:10.1002/adfm.201404511

Hockel, M., and Vaupel, P. (2001). Tumor hypoxia: Definitions and current clinical, biologic, and molecular aspects. *JNCI J. Natl. Cancer Inst.* 93 (4), 266–276. doi:10.1093/jnci/93.4.266

Huang, B., Chen, S., Pei, W., Xu, Y., Jiang, Z., Niu, C., et al. (2020). Oxygen-sufficient nanoplatform for chemo-sonodynamic therapy of hypoxic tumors. *Front. Chem.* 8, 358. doi:10.3389/fchem.2020.00358

Huang, P., Qian, X., Chen, Y., Yu, L., Lin, H., Wang, L., et al. (2017). Metalloporphyrin-encapsulated biodegradable nanosystems for highly efficient magnetic resonance imaging-guided sonodynamic cancer therapy. *J. Am. Chem. Soc.* 139 (3), 1275–1284. doi:10.1021/jacs.6b11846

Hussain, T., and Nguyen, Q. T. (2014). Molecular imaging for cancer diagnosis and surgery. *Adv. Drug Deliv. Rev.* 66, 90–100. doi:10.1016/j.addr.2013.09.007

Liu, J., Feng, L., and Wu, Y. (2021). Enzymatically synthesised MnO2 nanoparticles for efficient near-infrared photothermal therapy and dual-responsive magnetic resonance imaging. *Nanoscale* 13 (25), 11093–11103. doi:10.1039/d1nr02400k

Liu, Z., Zhang, S., Lin, H., Zhao, M., Yao, H., Zhang, L., et al. (2018). Theranostic 2D ultrathin MnO2 nanosheets with fast responsibility to endogenous tumor microenvironment and exogenous NIR irradiation. *Biomaterials* 155, 54–63. doi:10.1016/j.biomaterials.2017.11.015

Ma, Z., Jia, X., Bai, J., Ruan, Y., Wang, C., Li, J., et al. (2017). MnO2Gatekeeper: An intelligent and O2-evolving shell for preventing premature release of high cargo payload core, overcoming tumor hypoxia, and acidic H2O2-sensitive MRI. *Adv. Funct. Mat.* 27 (4), 1604258. doi:10.1002/adfm.201604258

Niu, C., Xu, Y., An, S., Zhang, M., Hu, Y., Wang, L., et al. (2017). Near-infrared induced phase-shifted ICG/Fe3O4 loaded PLGA nanoparticles for photothermal tumor ablation. *Sci. Rep.* 7 (1), 5490. doi:10.1038/s41598-017-06122-1

Pei, W., Huang, B., Chen, S., Wang, L., Xu, Y., and Niu, C. (2020). <p>Platelet-Mimicking drug delivery nanoparticles for enhanced chemo-photothermal therapy of breast cancer</p>. *Int. J. Nanomedicine* 15, 10151–10167. doi:10.2147/IJN.S285952

Qian, X., Zheng, Y., and Chen, Y. (2016). Micro/nanoparticle-augmented sonodynamic therapy (SDT): Breaking the depth shallow of photoactivation. *Adv. Mat.* 28 (37), 8097–8129. doi:10.1002/adma.201602012

Rosenthal, I., Sostaric, J. Z., and Riesz, P. (2004). Sonodynamic therapy--a review of the synergistic effects of drugs and ultrasound. *Ultrason. Sonochem.* 11 (6), 349–363. doi:10.1016/j.ultsonch.2004.03.004

Son, S., Kim, J. H., Wang, X., Zhang, C., Yoon, S. A., Shin, J., et al. (2020). Multifunctional sonosensitizers in sonodynamic cancer therapy. *Chem. Soc. Rev.* 49 (11), 3244–3261. doi:10.1039/c9cs00648f

Song, G., Liang, C., Yi, X., Zhao, Q., Cheng, L., Yang, K., et al. (2016). Perfluorocarbon-loaded hollow Bi2Se3 nanoparticles for timely supply of oxygen under near-infrared light to enhance the radiotherapy of cancer. *Adv. Mat.* 28 (14), 2716–2723. doi:10.1002/adma.201504617

Song, X., Feng, L., Liang, C., Yang, K., and Liu, Z. (2016). Ultrasound triggered tumor oxygenation with oxygen-shuttle nanoperfluorocarbon to overcome hypoxia-associated resistance in cancer therapies. *Nano Lett.* 16 (10), 6145–6153. doi:10.1021/acs.nanolett.6b02365

Sun, W., Yu, H., Wang, D., Li, Y., Tian, B., Zhu, S., et al. (2021). MnO2 nanoflowers as a multifunctional nano-platform for enhanced photothermal/photodynamic therapy and MR imaging. *Biomater. Sci.* 9 (10), 3662–3674. doi:10.1039/d1bm00033k

Wan, G. Y., Liu, Y., Chen, B. W., Liu, Y. Y., Wang, Y. S., Zhang, N., et al. (2016). Recent advances of sonodynamic therapy in cancer treatment. *Cancer Biol. Med.* 13 (3), 325–338. doi:10.20892/j.issn.2095-3941.2016.0068

Wang, L., Chen, S., Zhu, Y., Zhang, M., Tang, S., Li, J., et al. (2018). Triple-modal imaging-guided chemo-photothermal synergistic therapy for breast cancer with magnetically targeted phase-shifted nanoparticles. *ACS Appl. Mat. Interfaces* 10 (49), 42102–42114. doi:10.1021/acsami.8b16323

Wang, X., Zhong, X., Gong, F., Chao, Y., and Cheng, L. (2020). Newly developed strategies for improving sonodynamic therapy. *Mat. Horiz.* 7 (8), 2028–2046. doi:10.1039/d0mh00613k

Wells, P. N. (2006). Ultrasound imaging. *Phys. Med. Biol.* 51 (13), R83–R98. doi:10.1088/0031-9155/51/13/R06

Wood, A. K., and Sehgal, C. M. (2015). A review of low-intensity ultrasound for cancer therapy. *Ultrasound Med. Biol.* 41 (4), 905–928. doi:10.1016/j.ultrasmedbio.2014.11.019

Wu, F., Wang, Z. B., Zhu, H., Chen, W. Z., Zou, J. Z., Bai, J., et al. (2005). Feasibility of US-guided high-intensity focused ultrasound treatment in patients with advanced pancreatic cancer: Initial experience. *Radiology* 236 (3), 1034–1040. doi:10.1148/radiol.2362041105

Xu, Y., Li, W., Chen, S., Huang, B., Pei, W., and Niu, C. (2020). Near-Infrared responsive phase-shifted nanoparticles for magnetically targeted MR/US imaging and photothermal therapy of cancer. *Front. Bioeng. Biotechnol.* 8, 599107. doi:10.3389/fbioe.2020.599107

Yang, X., Yang, Y., Gao, F., Wei, J. J., Qian, C. G., and Sun, M. J. (2019). Biomimetic hybrid nanozymes with self-supplied H(+) and accelerated O2 generation for enhanced starvation and photodynamic therapy against hypoxic tumors. *Nano Lett.* 19 (7), 4334–4342. doi:10.1021/acs.nanolett.9b00934

Zhang, L., Yi, H., Song, J., Huang, J., Yang, K., Tan, B., et al. (2019). Mitochondria-targeted and ultrasound-activated nanodroplets for enhanced deep-penetration sonodynamic cancer therapy. *ACS Appl. Mat. Interfaces* 11 (9), 9355–9366. doi:10.1021/acsami.8b21968

Zhang, Y., Xu, Y., Sun, D., Meng, Z., Ying, W., Gao, W., et al. (2020). Hollow magnetic nanosystem-boosting synergistic effect between magnetic hyperthermia and sonodynamic therapy via modulating reactive oxygen species and heat shock proteins. *Chem. Eng. J.* 390, 124521. doi:10.1016/j.cej.2020.124521

Zhang, Z., and Ji, Y. (2020). Nanostructured manganese dioxide for anticancer applications: Preparation, diagnosis, and therapy. *Nanoscale* 12 (35), 17982–18003. doi:10.1039/d0nr04067c

Zhu, P., Chen, Y., and Shi, J. (2018). Nanoenzyme-augmented cancer sonodynamic therapy by catalytic tumor oxygenation. *ACS Nano* 12 (4), 3780–3795. doi:10.1021/acsnano.8b00999